Core and shallow-core d- to f-shell excitations in rare-earth metals

J. A. Bradley, K. T. Moore, G. van der Laan, J. P. Bradley, and R. A. Gordon

Core and shallow-core *d* to *f* excitations in rare earth metals

J. A. Bradley[1*], K. T. Moore[1], G. van der Laan[2], J. P. Bradley[3], and R. A. Gordon[4]

[1] *Condensed Matter and Materials Division, Lawrence Livermore National Laboratory, Livermore, CA 94550*
[2] *Diamond Light Source, Chilton, Didcot OX11 0DE, United Kingdom*
[3] *Institute of Geophysics and Planetary Physics, Lawrence Livermore National Laboratory, Livermore, CA 94550*
[4] *PNCSRF, Dept. of Physics, Simon Fraser University, Burnaby, BC, Canada V5A 1S6*

Abstract

We report on the results of probing the light lanthanide metals Ce, Pr, and Nd with inelastic x-ray and electron scattering. Transmission electron microscope-based electron spectroscopy and nonresonant inelastic x-ray scattering are shown to be in a high degree of accord, and here serve as complementary probes of electronic structure. The high resolution and high signal-to-noise electron technique allows for the measurement of the complex and subtle excitation spectra in the lanthanide metals, validating the applicability of the screened trivalent atomic model used for these materials. In addition, the momentum transfer dependence of the x-ray scattering is extracted and compared against atomic calculations for the most tightly bound excitonic resonances, which provides a direct test of the predicted atomic radial wave functions.

*corresponding author: bradley41@llnl.gov

I. INTRODUCTION

Rare earth elements are integral components in a wide range of technologies, including wind turbines, hybrid car engines, and lasers. Not coincidentally, these applications often critically depend on the novel properties of the rare earth $4f$ electrons, properties that are derived primarily from their anisotropic spatial profile and ability to transform between localized and itinerant behavior. The mechanism responsible for $4f$ electron delocalization is contested [1-7] and likely varies by material. This delocalization and the phenomena of intermediate valence, where electrons exist in coherent superpositions of f-electron occupancy, are intrinsically mixed, yielding strong electronic correlations for many rare earth-based materials. However, at ambient pressure the light rare earth metals, Ce, Pr, and Nd, are an appealing base case. They are typically treated as trivalent ions containing 1, 2, or 3 localized $4f$ electrons, respectively, with an itinerant valence band composed of electrons of mixed (spd) symmetry, largely serving to screen the nuclear charge.

However, the borderline between atomic and collective behavior in rare earth metals is often thin, even nearby these seemingly simple cases. Alloying (chemical substitution), pressure, and temperature can effectively tune the $4f$ electron localization, turning the eigenstates of the system into admixtures of atomic-like states with corresponding admixtures of f-electron occupancy. In particular, Ce, Pr, and Nd metals exhibit a trend of pressure-driven volume collapses—from large (Ce, 15%) to moderate (Pr, 9%) to none at all (Nd)—related to $4f$ electron delocalization [3, 6, 8-19]. The character of this delocalization may be substantially different in each material, and the x-ray scattering used here promises to be an important probe for relevant high-pressure work. First however, the response of the ambient systems has to be fully characterized and understood.

Resonant and nonresonant x-ray emission spectroscopies have been used to study the lanthanide volume collapse with some success [4, 5, 20]. However, recent work has shown the value of two other, related inelastic scattering techniques for f-electron interrogation of rare earth materials—nonresonant inelastic x-ray scattering (NIXS) and electron energy loss spectroscopy (EELS) [21-26]. These are complementary probes that, when combined with theory, provide observables related to the electronic structure,

including *f*-occupancy, bond character, and orbital character [20, 24-29]. Compared to the L-edge x-ray emission spectroscopy, shallow-core NIXS & EELS has the advantage of being sensitive to spectral structure that is intrinsically much sharper, which promises to clarify interpretation. However for NIXS, this advantage comes the price of significantly reduced scattering cross section (~10^5 by comparison for rare earth materials), but the NIXS experiments can be performed, thanks to high flux synchrotron sources and advanced instrumentation. However, important classes of rare earth materials have yet to be investigated with NIXS even at ambient pressure, most notably the elemental metals. Here we present such an investigation of the light rare earth metals Ce, Pr, and Nd.

This paper progresses as follows: We show the strong applicability of the multiplet model for predicting the $4d \rightarrow 4f$ spectral excitation structure of the three lightest rare earth metals, which can be directly tied to the conventional atomic picture, modeling Ce, Pr and Nd with ground state $4f$ occupations of 1, 2 and 3, respectively. The EELS spectra are shown to contain a highly structured, fine mesh of peaks, all perfectly predicted. The NIXS spectra are presented and shown to be in a similarly impressive accord with multiplet theory, for excitations from both the $4d$ and $3d$ core shell (the $N_{4,5}$ and $M_{4,5}$ edges, respectively). However, the electronic excitation structure is a characteristic function of both energy and momentum transfer, so we present comparisons of the momentum transfer dependence as well. As is discussed in some detail, the results confirm the general treatment of these materials, and validate atomic predictions of the radial matrix elements. We then conclude.

II. EXPERIMENTAL

All NIXS measurements were performed with the lower energy resolution inelastic x-ray scattering (LERIX) spectrometer [30] at sector 20-ID-B of the Advanced Photon Source. Incident energy selectivity was accomplished with a double-bounce Si(111) monochromator, providing ~1.4 eV FWHM energy resolution. Spectrometer operation and performance were consistent with previous work [21, 25, 31, 32]. EELS measurements were acquired using a TITAN electron microscope with a monochromatic electron. Spectra were acquired from sample regions with a thickness of 30 +/- 10 nm,

ensuring spectra with little plural scattering. An objective aperture was employed that allowed the 000 and first-order reflections to contribute to the spectra, but removed higher-angle scattering, optimizing the peak to background. Generally, EELS spectra were acquired and processed in a manner similar to that described for other *f*-electron materials [33].

Great care was taken to avoid any oxidation of the highly reactive metal foils. For the NIXS measurements, 1 mm-thick foils (Alpha Aesar, 99.9%) were freshly cut, then immediately mounted and sealed, cut side up, in a sample container under flowing He (~10 cc container volume). This mount was then placed inside a larger environment (a few thousand cc) that was also sealed and under flowing He. For the EELS experiments, the foil samples were sanded, polished, dimpled and then milled with Ar ions (4.5 keV) until a tiny hole (~tens of microns) was visible under a microscope. EELS samples were then transferred in air to a vacuum-transfer chamber, evacuated, and brought directly to the microscope. For NIXS measurements, samples were exposed to air for less than 30 seconds, and for EELS measurements air exposure was a few minutes. This amount of exposure to air is known to produce at most 1-2 nm of oxide on each side of the TEM sample surface, since the ion-milling passivates the metal surface, inhibiting reactivity [34, 35]. Furthermore, all EELS samples were evaluated in situ by comparing the lanthanide fluorescence intensity to the oxygen K-α fluorescence intensity and were deemed to be highly pure metals.

III. THEORY

For incident photon energies far away from resonant excitation and with scattering in the Born approximation (both conditions are fulfilled in the work presented here) the double differential cross section (DDCS) for inelastic x-ray and inelastic electron scattering can be described by the following expression (in atomic units)

$$\frac{d^2\sigma}{d\Omega d\omega} = \left(\frac{d\sigma}{d\Omega}\right)_{Exp} S(\mathbf{q},\omega), \qquad (1)$$

with

$$S(\mathbf{q},\omega) = \sum_f |\langle f | \sum_a e^{i\mathbf{q}\cdot\mathbf{r}_a} |i\rangle|^2 \, \delta(E_i - E_f + \omega)$$

, (2)

where ω is the energy loss by the incident photon (electron), $|i\rangle$ and $\langle f|$ are the initial and final multi-electronic states of the target (with associated energies E_i and E_f), $\mathbf{q}$ is the momentum transfer in the excitation process. The $\mathbf{r}_a$ represents the single-electron position vector, but in the following we will omit the subscript a, and implicitly assume summation over different electrons. The factor $(d\sigma/d\Omega)_{Exp}$ in Eq. (1) gives either the Thomson photon or the Rutherford electron cross section which can be factored out of the DDCS, so for each technique the results can be transformed into the *dynamic structure factor*, $S(\mathbf{q},\omega)$, which is independent of the specific experiment.

At low momentum transfer, as is the case for the EELS experiments reported here, the exponential operator can be approximated by the dipole operator, $i\mathbf{q}\cdot\mathbf{r}_a$, and the excitation structure probed is identical to that of x-ray absorption (with linearly polarized photons), where $\hat{\mathbf{q}}$ plays the role of the x-ray polarization vector in XAS [20, 31, 36-42].

At larger momentum transfer, the dipole approximation fails, and the transition operator $e^{i\mathbf{q}\cdot\mathbf{r}}$ may be expanded in spherical harmonics, which are an appropriate basis for an atomic treatment. The matrix element for a given final state, satisfying the energy delta function, becomes

$$\langle f | \, e^{i\mathbf{q}\cdot\mathbf{r}} \, |i\rangle = \sum_{k,\kappa} i^k (2k+1) C_\kappa^{(k)*}(\hat{\mathbf{q}}) A_\kappa^{(k)}(\hat{\mathbf{r}}), \quad (3)$$

where $C_\kappa^{(k)}(\hat{r}) = \sqrt{4\pi/(2k+1)}Y_\kappa^{(k)}(\hat{r})$, in which $Y_\kappa^{(k)}(\hat{r})$ is the familiar spherical harmonic and j_k is the kth order spherical Bessel function. The factor $A_\kappa^{(k)}$ is defined as

$$
\begin{aligned}
A_\kappa^{(k)}(\hat{\mathbf{r}}) &\equiv \langle f \,| j_k(qr) \, C_\kappa^{(k)}(\hat{\mathbf{r}}) \,|i\rangle \\
&= \langle R_{n'\ell'}^f \,| j_k(qr) \,| R_{n\ell}^i \rangle \langle \psi_{\ell'm'}^f \,| C_\kappa^{(k)}(\hat{\mathbf{r}}) \,| \psi_{\ell m}^i \rangle
\end{aligned}, \quad (4)
$$

with $m' = m + \kappa$ and where in the last step the initial and final state wave functions have been factored into radial and angular parts.

These expressions provide some intuition. The $C_\kappa^{(k)}$ transition operators are simply a generalization of the dipole transition that occurs at low momentum transfer. In general, as momentum transfer increases, first dipole (k=1), then quadrupole (k=2), octupole (k=3) and higher order electronic transitions ascend in likelihood, each maximizing within the experimental cross section in sequence [21, 25, 26, 29, 37]. The result is *q*-variation in selection rules, with concomitant variation in the final states probed through the scattering process.

In principle these channels may interfere: Substituting Eq. (3) into Eq. (2) gives

$$S(\mathbf{q},\omega)_{f,i} = \sum_{k,k',\kappa,\kappa'} i^{k-k'} (2k'+1)(2k+1)\, C_{\kappa'}^{(k')}(\hat{\mathbf{q}}) C_\kappa^{(k)*}(\hat{\mathbf{q}}) A_{\kappa'}^{(k')*}(\hat{\mathbf{r}}) A_\kappa^k(\hat{\mathbf{r}})$$

$$, \quad (5)$$

which shows interference terms ($k \neq k'$). along with the pure multipole transitions ($k = k'$). However, due to the orthogonality condition of the spherical harmonics, $\int C_{\kappa'}^{(k')*}(\hat{\mathbf{q}}) C_\kappa^{(k)}(\hat{\mathbf{q}}) = 4\pi(2k+1)^{-1}\delta_{kk'}\delta_{\kappa\kappa'}$, the interference terms vanish when the angular intensity is integrated over all directions $\hat{\mathbf{q}}$, in the same way as in, e.g., angular dependent photoemission [43]. This average neglects anisotropy due to the crystalline lattice, which have effects even in the limit of an average over many small, randomly distributed polycrystals [44,45]. The limits of this approximation will be discussed in the analysis, but for now we proceed using it. Integrating over the total angular distribution we can write Eq. (5) as

$$S(\mathbf{q},\omega)_{f,i} = 4\pi \sum_k |\langle R_{n'\ell'}^f | j_k(qr) | R_{n\ell}^i \rangle|^2 |\langle \psi_{\ell'}^f \| C^{(k)}(\hat{\mathbf{r}}) \| \psi_\ell^i \rangle|^2$$

$$, \quad (6)$$

where we assume isotropic sample conditions, so that summing over *m* and *m'* gives the reduced matrix elements, $\langle f \| C^{(k)} \| i \rangle$. The radial matrix elements, which contain the *q*-dependence, strongly depend on the specific core–valence transition, but are a slowly varying function over the energy range of the spectrum. By taking the radial matrix element as energy independent, it can be factored out of the sum over the final states, and the 2^k-pole spectra can be calculated independent of *q*.

The angular matrix element in Eq. (6) shows that the allowed multipole moments k for the $n\ell \rightarrow n'\ell'$ transition are restricted by the triangle condition, $|\ell - \ell'| \le k \le \ell + \ell'$, with parity, $\ell + \ell' + k =$ even. Thus for $d \rightarrow f$ transitions, only $k = 1$ (dipole), $k = 3$ (octupole), and $k = 5$ (triakontadipole) transitions are allowed.

Using atomic multiplet theory, we calculated the allowed transition probabilities for the $k = 1$, $k = 3$, and $k = 5$ spectra for $3d$ and $4d$ excitations in the trivalent Ce f^1, Pr f^2, and Nd f^3 ions [46]. The wave functions of the initial- and final-state configurations were calculated in intermediate coupling using Cowan's atomic Hartree-Fock (HF) code with relativistic correction [47]. Angle-integrated electric 2^k-pole transitions were calculated in spherical symmetry from the initial state $4f^n$ to the final state levels of the $4d^9 4f^{n+1}$ and $3d^9 4f^{n+1}$ configurations. The Hartree Fock values of the Slater parameters were reduced to 80% to account for screening effects, as was previously found to be the optimal value for the rare earths $M_{4,5}$ x-ray absorption [48]. Since such an 80% scaling has become standard for rare earths [46], there are essentially no free parameters in the calculation.

The average energy of the configurations was shifted to coincide with the measured spectra. Note that the three different k spectra are not shifted with respect to each other in any case reported here. The calculated $M_{4,5}$ spectra were broadened as in previous work [48]. The calculated $N_{4,5}$ spectra were convolved with a Lorentzian of half-width $\Gamma = 0.1$ eV for the intrinsic line width and a Gaussian of $\sigma = 0.1$ eV (for $k = 1$) and $\sigma = 0.3$ eV (for $k = 3$ and 5) to make for a visually clearer comparison to experiments, where there is instrumental broadening. In the $k = 1$ spectrum of the $N_{4,5}$ spectra the broadening was optimized for the pre-edge structure in the EELS spectra. A good agreement for the giant resonance region can be obtained by convolving the main peaks with a Fano line shape of half-width of 4-6 eV and an asymmetry parameter of 4-2.5 [34]. It should be noted that the energy resolution for the $k = 3$ and $k = 5$ $N_{4,5}$ NIXS spectra is primarily limited by the instrumental broadening and not by the intrinsic line width, which should be the same for all k spectra.

IV. RESULTS AND DISCUSSION

A. The $N_{4,5}$ spectra

Dipole-restricted EELS measurements, q-dependent NIXS results and calculated multipole spectra for Ce $N_{4,5}$ ($4d \rightarrow 4f$) are compared in Fig. 1. Ce EELS measurements have been reported previously [34] and are included here for completeness and to highlight the agreement with the low-q NIXS measurement. Since the chemical purity of the Ce was verified *in-situ* using x-ray fluorescence during the EELS measurements, the NIXS-EELS agreement validates that the NIXS measurements probed metallic Ce. For further validation, consider the strong agreement between the high-q NIXS and the predicted peak structure for the $k = 3$ and $k = 5$ transitions. For Ce, the spectral structure below 115 eV (the *pre-threshold* region) has been shown to be strongly and predominantly dependent on the f-electron occupancy [21]. Both this dependence and the high degree of accuracy of the atomic multiplet calculations are consequences of the highly localized nature of the final states in the pre-threshold region, which contains a $4d$ hole and an extra $4f$ electron. The interactions between the $4f$ orbitals and the environment (such as crystalline electric field and hybridization with the delocalized *spd* band electrons) are reduced due to this localization. The lower-energy final states have higher values of the orbital angular momenta, and are only visible in the dipole spectrum through mixing by the spin-orbit interaction [23]. For higher order multipole transitions, however, the pre-threshold states are allowed and provide a fingerprint of the f-electron occupancy, visible to NIXS and well explained by theory, as is shown [21-23, 25, 34]. By contrast, the higher energy spectral structure (>115 eV) is influenced by more extended final states that interact with the continuum bands, giving rise to Fano resonances and clearly leaving the ionic limit [29, 49-52].

The excellent conformity of the pre-threshold transitions to the atomic multiplet treatment is demonstrated in Fig. 2, where high-resolution EELS and calculated $4d$ spectra are compared for Ce, Pr, and Nd. The agreement is striking, given the large number of peaks with their irregular structure and the parameter-free approach of the calculation.

The NIXS and EELS $4d$-excitation spectra in Figs. 3 and 4 for Pr and Nd, respectively, are compared to theory in the dipole limit ($k = 1$), and the high momentum

transfer NIXS is compared to the calculated $k = 3$ and $k = 5$ spectra. The resulting agreement for the higher multipole transitions is again excellent.

B. The $M_{4,5}$ spectra

The $3d \rightarrow 4f$ spectra ($M_{4,5}$ edges) for all three elements are shown in Fig. 5 and are also in excellent agreement with the theoretical dipole spectra. The calculation closely matches the XAS in Thole *et al.* [48], which has an instrumental broadening of $\sigma = 0.25$-0.3 eV. The instrumental resolution of the EELS is somewhat broader ($\sigma = 0.35$-0.4 eV) in line with expectations, while that of the NIXS is ~1.4 eV FWHM. The total $3d^9 4f^{n+1}$ multiplet structure (disregarding selection rules) covers a very broad energy range (10-20 eV for each spin-orbit split peak—see Thole [48]). However, selection rules greatly reduce the number of final states that can be reached from the initial state. As shown in Fig. 3 the calculated $k = 3$ and $k = 5$ spectra display final states at distinctly different energy positions. Comparison to the experimental NIXS provides no evidence that these spectra contain significant amounts of higher multipole contributions. The absence of these higher multipole contributions can be ascribed to the smaller radius of the $3d$ orbital, compared to the $4d$, which shifts the maximum intensity of the individual multipole transitions to higher q, meaning that the region where $k = 3$ and $k = 5$ scattering is dominant is also a region of very low NIXS intensity. The EELS data is also a fairly faithful representation of the dipole spectrum, but even so, the EELS need not be completely immune to higher multipole transitions, and comparison of spectral shape to theory could support some very slight multipole influence on the EELS spectra.

C. The q-dependence of the multipole spectra

Given the good agreement obtained for the spectral structure, we decompose in Fig. 6 the Ce pre-threshold region into $k = 3$ and $k = 5$ components via a fitting procedure. Such a treatment assumes the absence of interference effects between the $k = 3$ and $k = 5$ terms in Eq. (5), which is a consequence of averaging over the direction of momentum transfer, as discussed above. By the quality of the fits, we judge this average

to be a reasonable approximation, however the small deviations between fit and experiment at ~112 eV energy loss could be related to the limitations of this treatment. To further investigate this, the orientation dependence of these resonances could be measured directly for a single crystal sample. Spectra for Ce were brought into absolute units of eV^{-1} using the Bethe sum rule, as described elsewhere [53], and a linear background was subtracted before fitting to the calculated multipole spectra to account for Compton scattering from the valence electrons over the ~10 eV pre-threshold region that was fitted.

Analogous results of fitting the calculated multipole spectra to the experimental spectra for Pr and Nd are not shown, but the results are of similar quality. Instead, in Fig. 7, we present the q-dependence of the integrated intensity of the multipole spectra as derived from the fits for Ce. The energy dependence of the dynamic structure factor agrees almost perfectly with theory, and as seen in Fig. 7 by comparing to previous work [54], atomic calculations predict the q dependence as well. The agreement in terms of q dependence, while good, does show a slight deviation from the calculation, especially for the lower multipole transitions. This is possibly due to the q averaging that leads to the approximation of vanishing interference between multipole channels, an approximation that is made inexact by the crystalline (non-spherical) symmetry of the lattice.

A less exotic explanation is possible as well. In the limit of non-interfering multipolar channels, equation (6) highlights the q dependence of $S(\mathbf{q},\omega)$, where q appears only in the radial integral. The q dependence thus provides a direct interrogation of the reliability of the $4d$ and $4f$ radial wave functions predicted by theory. The modest differences between the predicted and measured q-dependence are therefore a possible consequence of electron screening effects, which play a major role in localized electron systems.

Extraction of the q-dependence requires a more involved experimental effort. To produce data like those in Fig. 8, the spectra at different q must be normalized into equivalent units. To do this with the Bethe sum rule, the instrumental response must be characterized over a large energy range (~3 keV) and the normalization integral, which is formally taken over an infinite region, must be handled appropriately. A detailed discussion of this procedure is included elsewhere [53], and the normalization for Ce was

done along these lines. Relative normalization uncertainty for Ce is 10-20% for most q values, but is worse at lowest q because of lowered signal due to details of the particular experimental geometry. Otherwise, the error schedule is similar to the previous work done on N_2 gas.

For comparison, we also present the q-dependence of the multipole spectra for Pr and Nd in Fig. 8. Smoothed curves are included as guides for the eye. Pr and Nd were normalized to the Ce data: The background valence Compton profile was made to overlap that of Ce by removal of a linear background and multiplicative rescaling of the data. The error induced by this procedure should be on the order of the relative difference in the number of electrons for the materials (i.e., 1/58 for Pr and 2/58 for Nd). Then the Compton profile itself was removed by a linear fit in the pre-threshold region. In all three cases, the dipole intensity was determined by integration of the signal over a small energy band of the GDR after removal of the linear background. The $k = 3$ and $k = 5$ intensities for Nd and Pr were determined by fitting, as in the case of Ce. While normalization is consistent for every q in a given multipolar channel, the relative normalization between the $k = 1$, $k = 3$, and $k = 5$ spectra is arbitrary, to optimize the visual presentation. The results show that the q-dependence of the different k spectra slightly varies for Ce, Pr, and Nd.

V. Conclusion

In this work we have presented inelastic electron and x-ray scattering results from the light rare earth metals Ce, Pr, and Nd, along with predictive calculations of the multipole spectra using an atomic approach. These metals at ambient pressure and temperature are taken as trivalent f-element metals, where the f-electron wave functions are supposed to be well described by an atomic model. In concert with this picture, we have shown that multiplet theory is capable of extremely accurate predictions of the spectra related to localized final states. Furthermore, we have demonstrated the extraction of the q-dependence of the different multipole spectra from appropriately normalized NIXS data through a fitting procedure based on the calculated spectra. The q-dependence is contained in the radial matrix element. In the case of these materials, we have seen that the q-dependence can be used as an independent means of evaluating our

understanding of the electronic wavefunctions, strongly validating the atomic treatment for all three of the light rare earth metals interrogated here.

Acknowledgements

Bibliography:

1.   J.W. Allen and R. M. Martin, Phys. Rev. Lett., **49**, 1106 (1982).
2.   B. Johansson, I. A. Abrikosov, M. Aldén , A. V. Ruban and H. L. Skriver Phys. Rev. Lett., **74**, 2335 (1995).
3.   A. K. McMahan, Phys. Rev. B, **72**, 115125 (2005).
4.   J. –P. Rueff, J. –P. Itié, M. Taguchi, C. F. Hague, J –M. Mariot, R. Delaunay, J. –P. Kappler, N. Jaouen, Phys. Rev. Lett., **96**, 237403 (2006).
5.   B. R. Maddox, A. Lazicki, C. S. Yoo, V. Iota, M. Chen, A. K. McMahan, M. Y. Hu, P. Chow, R. T. Scalettar, and W. E. Pickett, Phys. Rev. Lett., **96,** 215701 (2006).
6.   M. J. Lipp, D. Jackson, H. Cynn, C. Aracne, W. J. Evans, and A. K. McMahan Phys. Rev. Lett. **101**, 165703 (2008).
7.   B. Johansson, A. V. Ruban, and I. A. Abrikosov, Phys. Rev. Lett., **102**, 189601 (2009).
8.   D. G. Koskimaki and K. A. Gschneidner Jr., in *Handbook on the Physics and Chemistry of Rare Earths*, edited by K. A. Gschneidner Jr. and L. R. Eyring North-Holland, Amsterdam, (1978), p. 337.
9.   J. S. Olsen, L. Gerward, U. Benedict, and J. P. Itié, Physica B & C **133B**, 129 (1985).
10.   Y. K. Vohra, S. L. Beaver, J. Akella, C. A. Ruddle, and S. T. Weir, J. Appl. Phys. **85**, 2451 (1999).
11.   H. K. Mao, R. M. Hazen, P. M. Bell, and J, Wittig, J. Appl. Phys. **52**, 4572 (1981).
12.   G. S. Smith and J. Akella, J. Appl. Phys. **53**, 9212 (1982).
13.   Y. C. Zhao, F. Porsch, and W. B. Holzapfel, Phys. Rev. B **52**, 134 (1995).
14.   G. N. Chesnut and Y. K. Vohra, Phys. Rev. B **62**, 2965 (2000).
15.   B. J. Baer, H. Cynn, V. Iota, C-S. Yoo, and G. Shen, Phys. Rev. B **67**, 134115 (2003).
16.   N. C. Cunningham, N. Velisavljevic, and Y. K. Vohra, Phys. Rev. B **71**, 012108 (2005).
17.   Akella, J. and Smith, G.S., J. Less-Common Met. **116,** 313 (1986).
18.   F. Decremps, L. Belhadi, D. L. Farber, K. T. Moore, F. Occelli, M. Gauthier, A. Polian, D. Antonangeli, C. M. Aracne-Ruddle, and B. Amadon, Phys. Rev. Lett. **106**, 065701 (2011).
19.   K.T. Moore, L. Belhadi, F. Decremps, D. L. Farber, J. A. Bradley, F. Occelli, M. Gautier, A. Polian, and C. M. Aracne-Ruddle, Acta Materialia 59 6007 (2011).
20.   J. –P. Rueff and A. Shukla, Rev. Mod. Phys. **82**, 847 (2010).
21.   R. A. Gordon, G. T. Seidler, T. T. Fister, M. W. Haverkort, G. A. Sawatzky, A. Tanaka, and T. K. Sham, Europhy. Lett., **81** (2), 26004 (2008).
22.   K. T. Moore, G. van der Laan, M. A. Wall, A. J. Schwartz, and R. G. Haire, Phys. Rev. B **76**, 073105 (2007)
23.   M. T. Butterfield, K. T. Moore, G. van der Laan, M. A. Wall, and R. G. Haire, Phys. Rev. B **77**, 113109 (2008)
24.   K. T. Moore and G. van der Laan, Rev. Mod. Phys., **81**, 235 (2009)

25. J. A. Bradley, S. Sen Gupta, G. T. Seidler, K. T. Moore, M. W. Haverkort, G. A. Sawatzky, S. D. Conradson, D. L. Clark, S. A. Kozimor, and K. S. Boland, Phys. Rev. B **81,** 193104 (2010).

26. R. Caciuffo, G. van der Laan, L. Simonelli, T. Vitova, C. Mazzoli, M. A. Denecke and G. H. Lander, Phys. Rev. B. **81**, 195104 (2010).

27. J. A. Bradley, G. T. Seidler, G. Cooper, M. Vos, A. P. Hitchcock, A. P. Sorini, C. Schlimmer, and K. P. Nagle, Phys. Rev. Lett. **105,** 053202 (2010).

28. J. A. Bradley, P. Yang, E. R. Batista, K. S. Boland, C. J. Burns, D. L. Clark, S. D. Conradson, S. A. Kozimor, R. L. Martin, G. T. Seidler, B. L. Scott, D. K. Shuh, T. Tyliszczak, M. P. Wilkerson, and L. E. Wolfsberg, J. Am. Chem. Soc. **132,** (39), 13914 (2010).

29. S. Sen Gupta, J. A. Bradley, M. W. Haverkort, G. T. Seidler, A. Tanaka and G. A. Sawatzky, Phys. Rev. B, **84** 075134 (2011).

30. T. T. Fister, G. T. Seidler, L. Wharton, A. R. Battle, T. B. Ellis, J. O. Cross, A. T. Macrander, W. T. Elam, T. A. Tyson and Q. Qian, Rev. Sci. Instrum. **77,** 063901 (2006).

31. T. T. Fister, F. D. Vila, G. T. Seidler, L. Svec, J. C. Linehan, and J. O. Cross, J. Amer. Chem. Soc. **130** (3), 925 (2008).

32. H. Sternemann, C. Sternemann, G. T. Seidler, T. T. Fister, A. Sakko, and M. Tolan, J. Synchrotron Radiat **15,** 162 (2008).

33. K. T. Moore, Micron **41**, 336 (2010)

34. K. T. Moore, B. W. Chung, S. A. Morton, A. J. Schwartz, J. G. Tobin, S. Lazar, F. D. Tichelaar, H. W. Zandbergen, P. Soderlind, and G. van der Laan, Phys. Rev. B, **69**, 193104 (2004).

35. K. T. Moore M. A. Wall, A. J. Schwartz, B.W. Chung, S. A. Morton, J. G. Tobin, S. Lazar, F. D. Tichelaar, H. W. Zandbergen, P. Soderlind, and G. van der Laan, Philosophical Magazine 84, 1039 (2004)

36. U. Bergmann, Ph. Wernet, P. Glatzel, M. Cavalleri, L. G. M. Pettersson, A. Nilsson, and S. P. Cramer, Phys. Rev. B, **66,** 092107 (2002)

37. J. A. Soininen, A. L. Ankudinov, and J. J. Rehr, Phys. Rev. B, **72**, 045136 (2005).

38. K. Hämäläinen, S. Galambosi, J. A. Soininen, E. L. Shirley, J. –P. Rueff, and A. Shukla, Phys. Rev. B **65,** 155111 (2002)

39. K. P. Nagle, G. T. Seidler, E. L. Shirley, T. T. Fister, J. A. Bradley and F. C. Brown, Phys. Rev. B **80,** 045105 (2009).

40. T. T. Fister, T. T. Fister, G. T. Seidler, E. L. Shirley, F. D. Vila, J. J. Rehr, K. P. Nagle, J. C. Linehan, and J. O. Cross, J. Chem. Phys. **129,** 044702 (2008).

41. J. A. Soininen, A Mattila, J. J. Rehr, and K. Hämäläinen, Journal of Physics-Condensed Matter **18** (31), 7327 (2006).

42. Y. Feng, J. A. Soininen, A. L. Ankudinov, J. O. Cross, G. T. Seidler, A. T. Macrander, J. J. Rehr and E. L. Shirley, Phys. Rev. B, **77,** 165202 (2008).

43. B. T. Thole and G. van der Laan, Phys. Rev. B **49**, 9613 (1994).

44. R. A. Gordon, M. W. Haverkort, S. Sen Gupta and G. A. Sawatzky, J. Phys. Conf. Ser. **190** 012047 (2009).

45. R. A. Gordon, G. T. Seidler, T. T. Fister, and K. P. Nagle, J. Elec. Spec. Retal. Phenom. **184** 220 (2011).

46. G. van der Laan, Lect. Notes Phys. **697**, 143 (2006).

47. R. D. Cowan, *The Theory of Atomic Structure and Spectra (University of California Press*, Berkeley, CA 1981).

48. B. T. Thole, G. van der Laan, J. C. Fuggle, G. A. Sawatzky, R. C. Karnatak, and J. M. Esteva, Phys. Rev. B 32, 5107 (1985).

49. J. L. Dehmer, A. F. Starace, U. Fano, J. Sugar, and J. W. Cooper, Phys. Rev. Lett. **26**, 1521 (1971).

50. J. Sugar, Phys. Rev. B **5**, 1785 (1972).

51. A. F. Starace, Phys. Rev. B **5**, 1773 (1972).

52. K. Starke et al., Phys. Rev. B **55**, 2672 (1997).

53. J. A. Bradley, A. Sakko, G. T. Seidler, A. Rubio, M. Hakala, K. Hämäläinen, G. Cooper, A. P. Hitchcock, K. Schlimmer, and K. P. Nagle, Phys. Rev. A, **84**, 022510 (2011)

54. M. W. Haverkort, A. Tanaka, L. H. Tjeng, and G. A. Sawatzky, Phys. Rev. Lett. **99,** 257401 (2007).

55. M. Inokuti, Rev. Mod. Phys. **43,** 297 (1971).
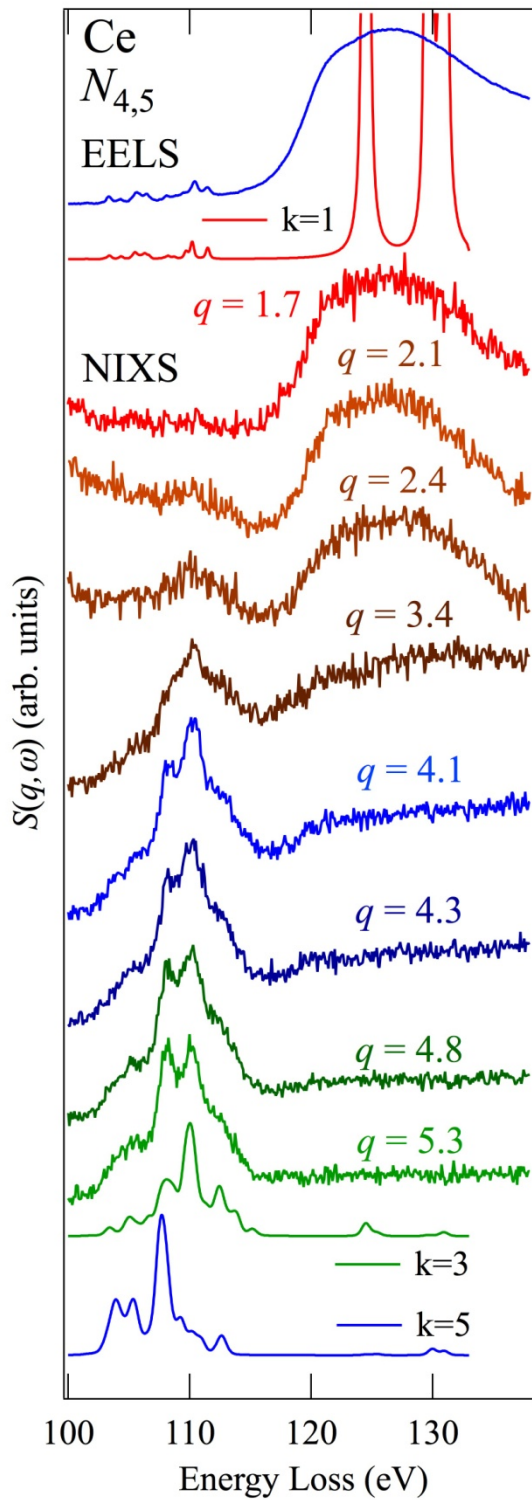
FIG. 1. (Color online) Core $4d$ to valence excitation spectra for Ce metal. TEM-based EELS is shown compared to the calculated $4d \rightarrow 4f$ electric dipole spectrum ($k = 1$). NIXS measurements are shown for a range of momentum transfer, and compared to

calculated multipole spectra ($k = 3$ and 5). Spectra are offset for clarity, and q is in atomic units.
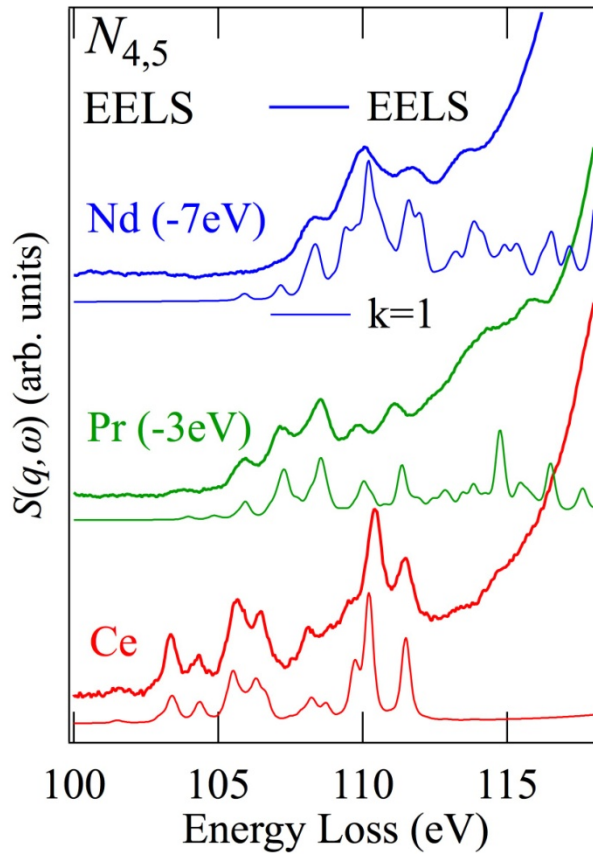
Fig. 2. (Color online) Close up view of the pre-threshold $4d$ excitation spectra for Ce, Pr and Nd. The complex multiplet structure for dipole excitation is in strong agreement with theory. Spectra are offset for clarity, and shifted in energy as indicated to allow presentation on the same plot.
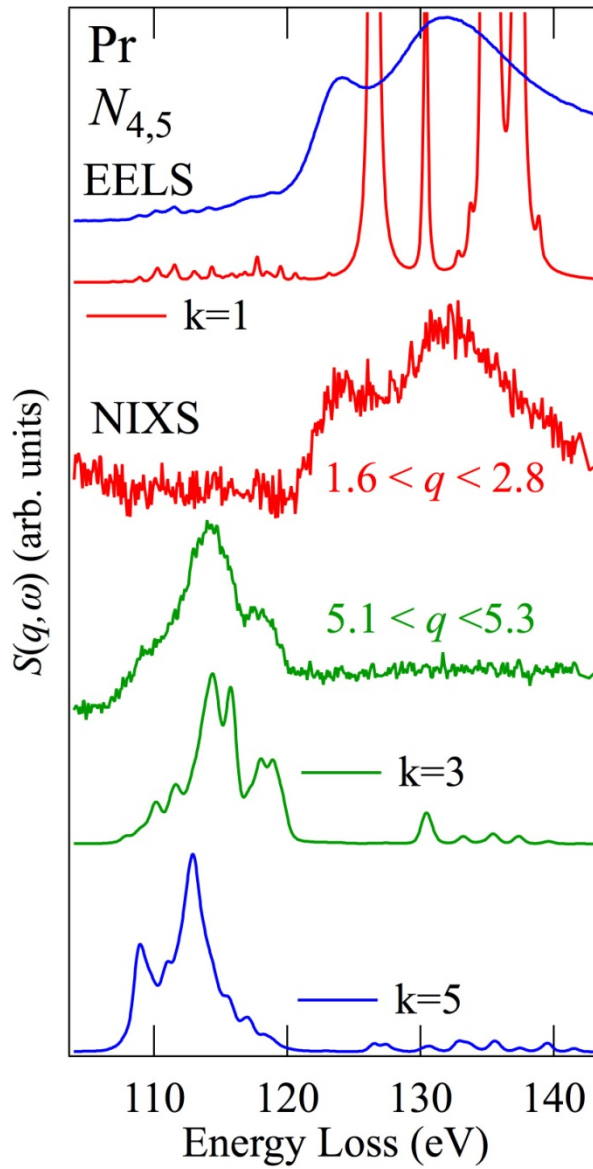
FIG. 3. (Color online) $4d$ to valence excitation spectra for Pr metal, taken with NIXS and EELS, and compared to the multipole spectra predicted by atomic multiplet theory for trivalent Pr. To enhance signal to noise, spectra from several different q values were averaged. Spectra are offset for clarity, and q is in atomic units.
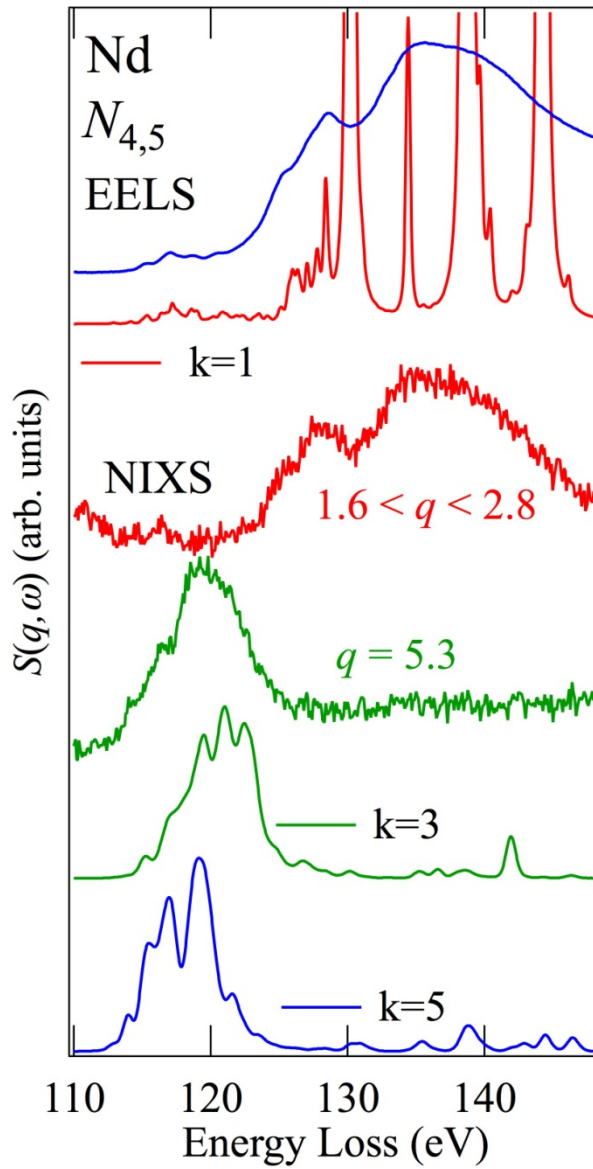
FIG. 4. (Color online) $4d$ to valence excitation structure for Nd metal, taken with NIXS and EELS, and compared to the multipole spectra predicted by atomic multiplet theory for trivalent Nd. To enhance signal to noise, spectra from several different q values were averaged. Spectra are offset for clarity, and q is in atomic units.
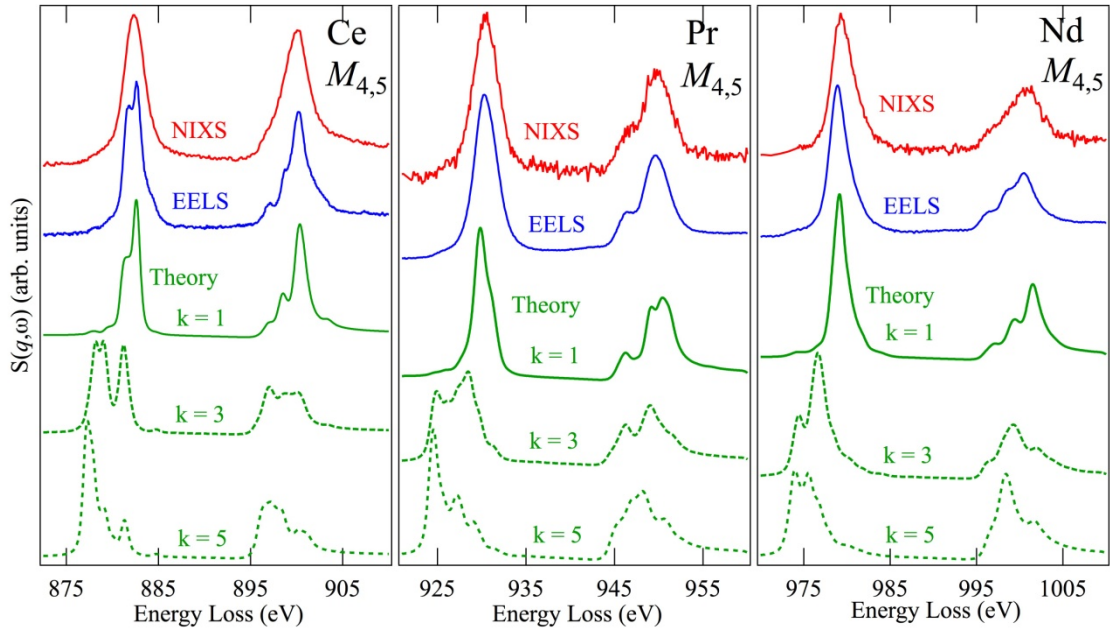
FIG. 5. (Color online) $3d$ to $4f$ ($M_{4,5}$) excitation spectra of Ce, Pr, and Nd measured by NIXS and EELS, compared to the predicted multipole spectra. The measured spectra are predominantly of dipolar ($k = 1$) character with little evidence of higher multipole spectra. The NIXS spectra shown represent an average over a range of q from 2.2 to 5.8 a.u.. Energy resolutions are 1.4 eV (NIXS) and 0.4 eV (EELS). Theoretical spectra have been broadened slightly less than the EELS resolution, and spectra are offset for clarity.
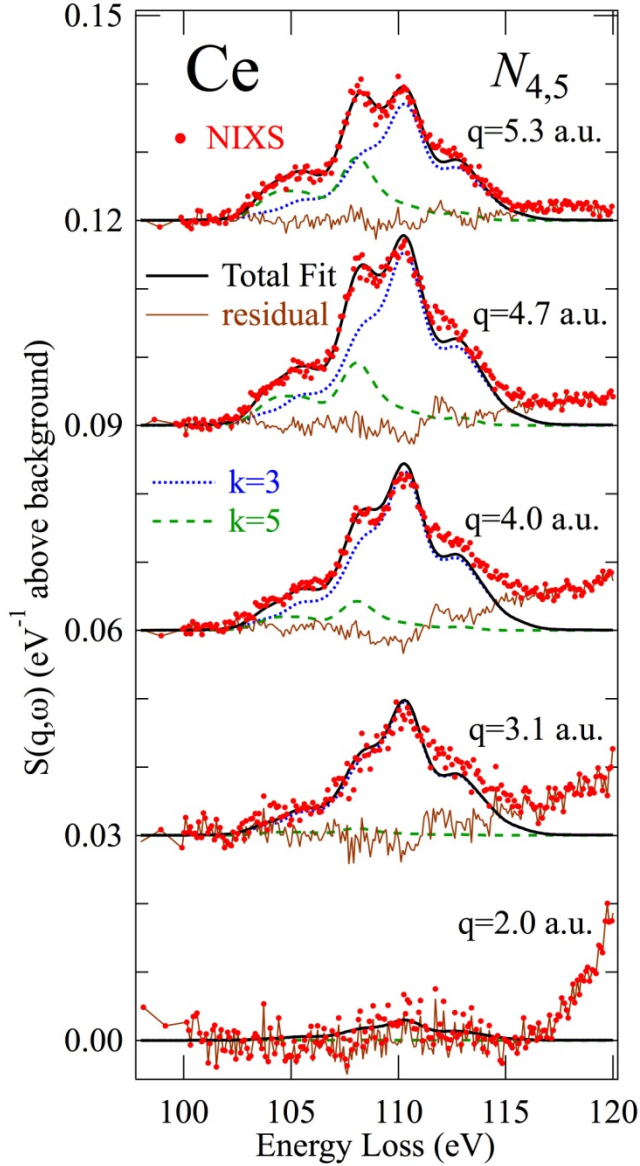
FIG. 6. (Color online) Decomposition of Ce $4d$ to valence ($N_{4,5}$) NIXS using the calculated higher multipole ($k = 3, 5$) spectra. Experimental data (dots) were brought into absolute units by applying the Bethe sum rule [53, 55], and the signal due to valence electron Compton scattering, approximated as linear over this energy range, was removed. This approximation is validated by general flatness of the residual (thin line). The spectra and fits (dashed and thick lines) are displayed for different momentum transfer, and are offset for clarity.
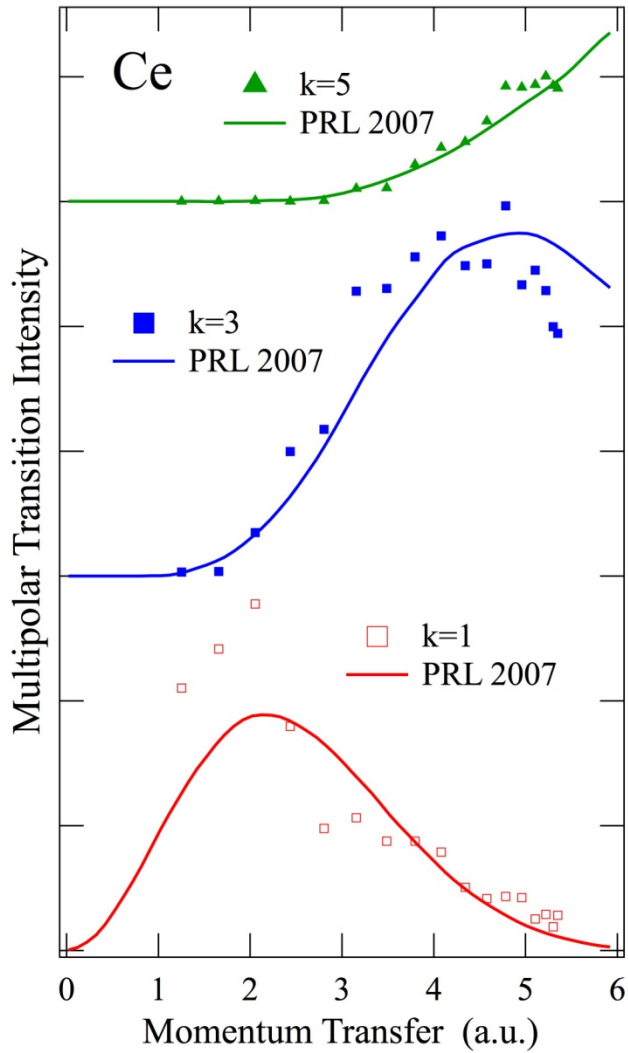
FIG. 7. Momentum transfer dependence of the multipolar transition intensities in Ce derived from the fits shown in Fig. 6. Since the experiment measures the squared matrix element [Eq. (2)], theoretical predictions as depicted in Haverkort *et al.* [54] have been squared. The $k = 1$ intensity is derived from an integral over a fixed region in energy loss, so the units are arbitrary. Because of this, and to compare shape explicitly, the theory is multiplicatively scaled to the data for each multipole. Curves are offset for clarity.
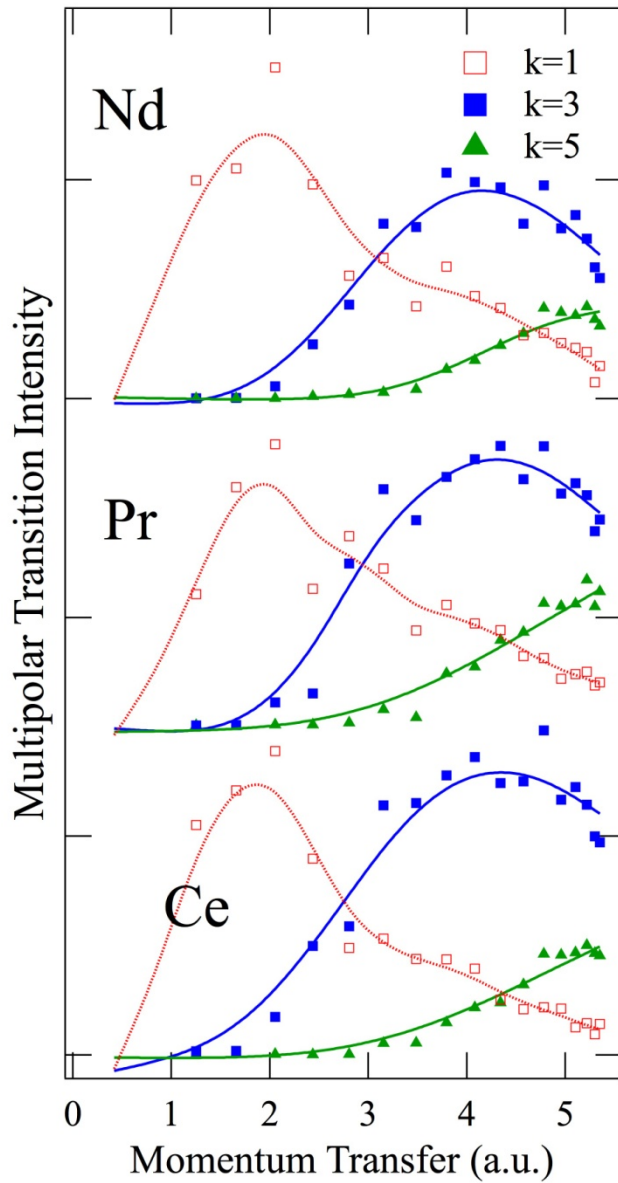
FIG. 8: Experimental determination of multipolar transition intensities for the three metals measured. As for Ce, the Pr and Nd energy loss spectra are brought into real units by the Bethe sum rule, and the $k = 3, 5$ intensities are derived from fits analogous to those shown in Fig. 6. Also, as for Ce, the dipole transition is determined by integration over a region in energy loss. In this figure, the curves are guides for the eye only, as they are derived by simply smoothing the data points. Pr and Nd results are offset for clarity.